THE JOURNAL OF PHYSICAL CHEMISTRY C
A JOURNAL OF THE AMERICAN CHEMICAL SOCIETY

pubs.acs.org/JPCC

Article

A Tale of Reactive Oxygen Species on the Ag_3PO_4(110) Surface

Felipe Lipsky, Luis Henrique da Silveira Lacerda, Lourdes Gracia, Beatriz G. Foschiani, Marcelo Assis, Mónica Oliva, Elson Longo, Juan Andrés,* and Miguel A. San-Miguel*

Cite This: *J. Phys. Chem. C* 2023, 127, 23235−23245

Read Online

ACCESS | Metrics & More | Article Recommendations | Supporting Information

ABSTRACT: Herein, we report a study of Ag_3PO_4 microcrystals in the accomplishment of their enhanced degradation process and bactericidal activity. Based on experimental results and density functional theory free energy profiles, we propose a new mechanism for the multifunctional competence of the Ag_3PO_4(110) surface. Coadsorbed H_2O and O_2 molecules regulate an energetically favorable pathway that efficiently activates the dissociation of H_2O and stabilizes the formed reactive oxygen species (ROS) precursors: hydroxyl (•OH) and superoxide ($•O_2^-$) radicals. This work is a proof of concept to interpret the surface reactions on Ag_3PO_4 and provides a new perspective to understand at the atomic level the catalytic process/mechanism for the initial stages of ROS production on metal oxide semiconductor surfaces.

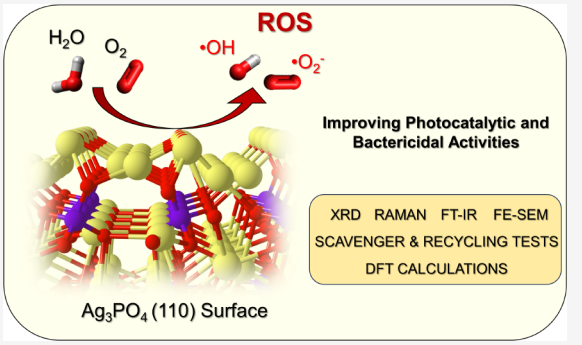

INTRODUCTION

The adsorption and activation of H_2O and O_2 molecules on the surfaces of inorganic semiconductors are of fundamental importance in numerous scientific and technological fields, including materials science, heterogeneous catalysis, and environmental applications.[1−3] The distinctive physical and chemical properties of these semiconductors result in different mechanisms, including the generation of reactive oxygen species (ROS) such as hydroxyl (•OH) and superoxide anion ($•O_2^-$) radicals when H_2O and O_2 are chemically absorbed on the exposed surfaces.[4,5]

The functionality of living cells heavily relies on ROS, which are actively involved in numerous physiological processes such as photosynthesis, cell signaling, inflammation, cytotoxicity, and respiration.[6−9] ROS are responsible for the oxidation of organic compounds, including those constituting the outer membrane of viruses, bacteria, or fungi, facilitating the targeted destruction of pathogens by oxidative stress.[10−12] Furthermore, they can gradually break down pollutants into smaller molecules that are safe and nontoxic and can be easily biodegraded.[13,14] This dual capability for pathogen eradication and pollutant detoxification holds tremendous potential for developing novel therapeutic strategies and solutions for environmental remediation. Nevertheless, ROS have a short diffusion distance once generated on the exposed surfaces (<50 nm);[15] consequently, dyes, cells, and tissues being targeted must be located nearby.

Ag_3PO_4 belongs to the Ag-based semiconductor family and has gained significant attention in recent years for its exceptional capacity for photocatalytic degradation of various organic dyes under visible-light irradiation, antimicrobial activity against a wide range of pathogens, surface-dependent bactericidal activity, outstanding photocatalytic oxidation performance, and remarkable chemical stability under different conditions.[16−22] Functionalization is facilitated by the flexible arrangement of metal and oxygen atoms on the exposed surfaces.

The crystal morphology of Ag_3PO_4 can be controlled through different synthesis conditions, such as pH and the addition of surfactants or solvents. These factors can change the surface chemical composition, the exposed surfaces, and the directions of growth, resulting in different structures and applications.[23−33] Ultimately, the design and synthesis of catalysts with a well-controlled morphology and well-defined exposed surfaces allow the investigation of the relationship between catalyst properties and surface reaction kinetics.

The generation of ROS in synthesized Ag_3PO_4 is regulated by the exposed crystal surfaces in its morphology,[34−37] which is primarily bound by the low-index (100), (110), and (111) crystallographic planes.[38−41] The findings presented in this summary highlight the suitability of the Ag_3PO_4-based materials for investigation purposes. However, we must stress that while the performance of these photocatalysts has been improved, the understanding of the generation of ROS on the Ag_3PO_4 surfaces has yet to evolve to the same degree, lacking detailed aspects of mechanisms and reaction pathways. In this work, we give a sustained and complete picture of a new

Received: September 21, 2023
Revised: November 2, 2023
Accepted: November 8, 2023
Published: November 20, 2023

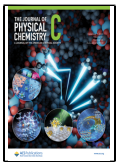

https://doi.org/10.1021/acs.jpcc.3c06321
J. Phys. Chem. C 2023, 127, 23235−23245

Scheme 1. Workflow Diagram

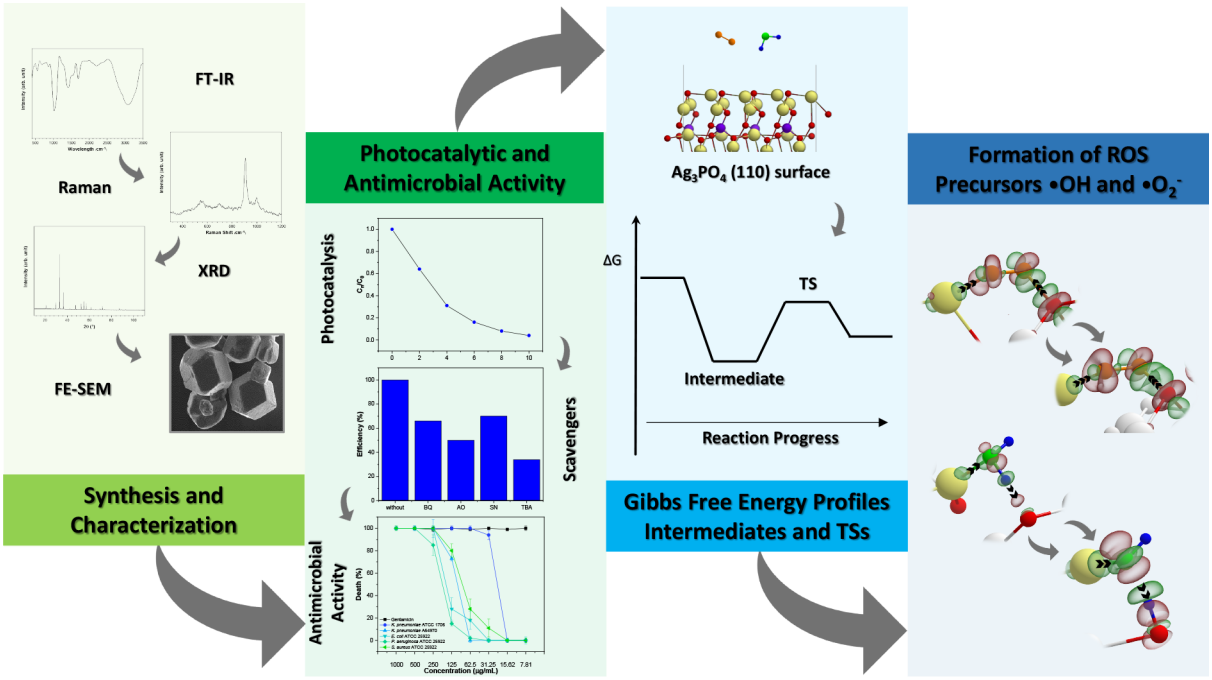

mechanism for the adsorption and activation of H_2O and O_2, which promotes the homolytic dissociation of these molecules at the $Ag_3PO_4(110)$ surface and leads to the precursors of ROS. The reason for its enhanced photocatalytic and bactericidal activities is discussed and explained.

Ag_3PO_4 microcrystals were synthesized by the coprecipitation method using NH_3 as a complexing agent and were characterized by using X-ray diffraction (XRD), Raman spectroscopy, and Fourier-transform infrared (FT-IR) spectroscopy. Field emission scanning electron microscopy (FE-SEM) images were employed to analyze the morphology of the as-synthesized crystals. We proved the enhanced photocatalytic degradation of Rhodamine B (RhB) in an aqueous solution under visible-light irradiation and the superior bactericidal activity against various strains (*Klebsiella pneumoniae* (*K. pneumoniae*) ATCC 1706, *K. pneumoniae* AS4970, *Escherichia coli* (*E. coli*) ATCC 25922, *Staphylococcus aureus* (*S. aureus*) ATCC 29213, and *Pseudomonas aeruginosa* (*P. aeruginosa*) ATCC 27853) by determining the minimum inhibitory concentrations (MIC). We used density functional theory (DFT) calculations to support and rationalize the experimental results to obtain the free energy reaction pathways. The corresponding stationary points were located and characterized to provide thermodynamic and kinetic data to better understand the chemical rearrangements and electron transfer processes on the $Ag_3PO_4(110)$ surface. We emphasized the atomic- and molecular-scale details of the active site structures required to enable the formation of relevant intermediates and transition states. The workflow of the present investigation is displayed in Scheme 1.

METHODS

Computations. Our calculations are based on density functional theory (DFT) with the generalized gradient approximation (GGA) of the Perdew–Burke–Ernzerhof (PBE) exchange–correlation functional.[42] The interactions between the valence electrons ($[Ag]4d^{10}5s^1$, $[P]3s^23p^3$, $[O]2s^22p^4$, and $[H]1s^1$) and the ionic cores are treated using the projector augmented wave potentials (PAW)[43,44] as implemented in the VASP code,[45,46] with an energy cutoff of 550 eV. In all calculations, we added the *a posteriori* Grimme D3 semiempirical van der Waals interaction correction with Becke–Johnson damping effects to account for the dispersion effects.[47]

We utilized the DFT-PBE functional due to computational limitations preventing the use of the more precise screened hybrid functional for transition state searches in surface slab calculations on the simulated supercells. Nonetheless, our DFT-PBE-based results matched the qualitative accuracy of surface Bader charges and density of states (DOS) computed with PBE+U[48] and HSE06[49] functionals (Section S2.3).

To accurately represent the experimental data, we chose convergence thresholds of 10^{-6} eV for the electronic self-consistent field cycle and 0.00005 eV/Å for the maximum Hellmann–Feynman forces for the bulk optimization and 10^{-5} eV and 0.01 eV/Å for the surface optimization. Brillouin zone integration was performed using the Γ-centered Monkhorst–Pack scheme with a grid of 7 × 7 × 7 (bulk) and 3 × 3 × 1 (surface) points and a Gaussian smearing of 0.01 eV. We switched to the tetrahedron method with Blöchl corrections[50] for the static calculations.

Structural optimization of gas-phase molecules (O_2 and H_2O) was performed using a 15 × 20 × 25 Å supercell with the Γ-point and energy and force convergence thresholds of 10^{-8} eV and 0.00001 eV/Å, respectively.

The DOS was analyzed with the VASPKIT tool,[51] and the crystal orbital Hamilton population (COHP) was obtained using the LOBSTER package.[52] Bader charges were evaluated through the code developed by Yu and Trinkle.[53] The electron density difference was computed by $\Delta\rho(x,y,z) = \rho(x,y,z)_{system} - \rho(x,y,z)_{slab} - \Sigma\rho(x,y,z)_{molecule}$, where ρ_{system} represents the total electron density of the adsorbate/substrate system. $\rho_{molecule}$ and ρ_{slab} denote the electron density of the adsorbate molecule and the substrate, respectively, in which their

https://doi.org/10.1021/acs.jpcc.3c06321
J. Phys. Chem. C 2023, 127, 23235−23245

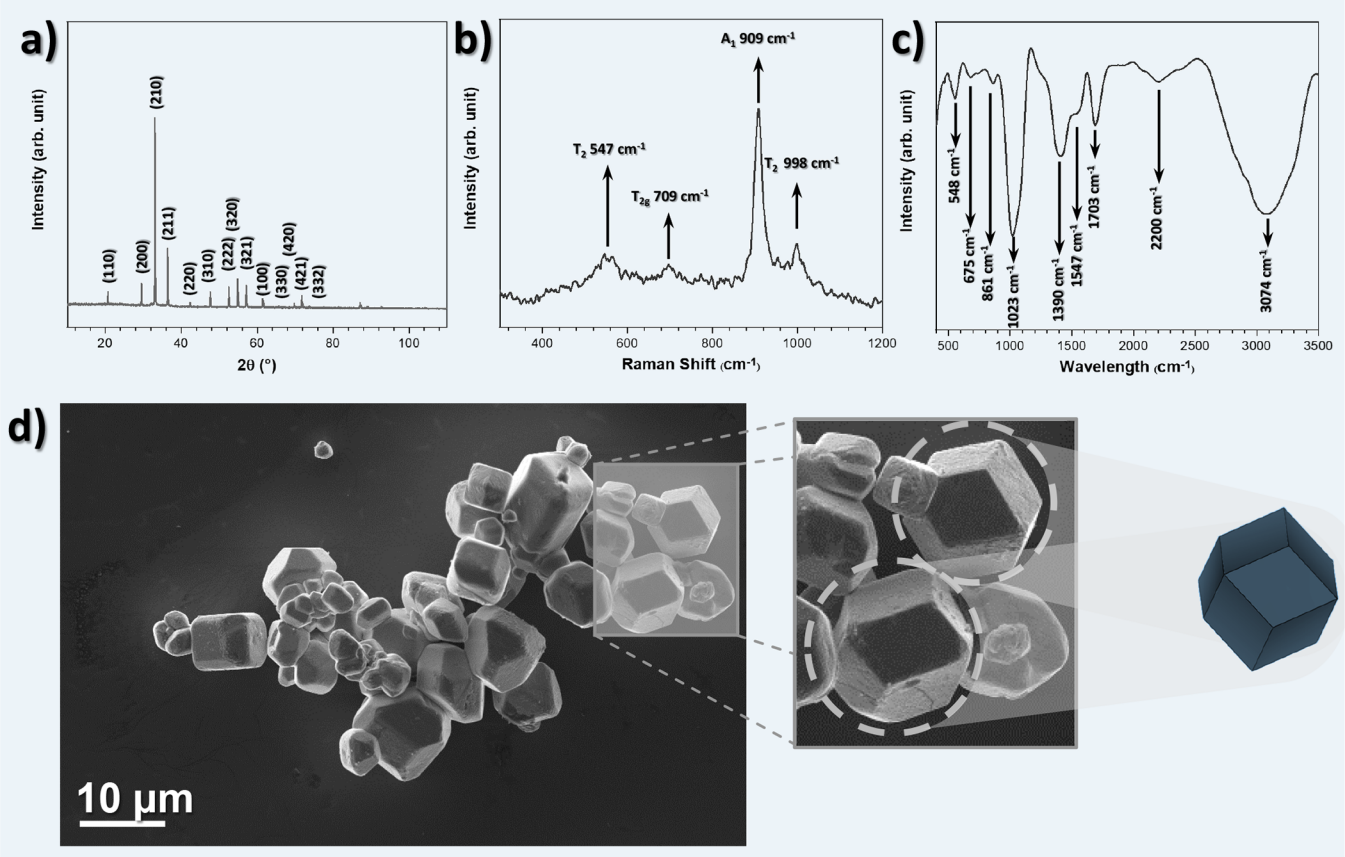

Figure 1. Structural characterizations of Ag_3PO_4 crystals. (a) XRD pattern, (b) Raman spectrum, (c) FT-IR spectrum, and (d) FE-SEM image of as-synthesized Ag_3PO_4 crystals with the rhombic dodecahedral morphology, composed mainly of the (110) surface.

positions were fixed at the adsorbed geometry. We performed a topological analysis of the surface's electronic density grid with AIM-UC[54] software.

Transition states (TS) were obtained using the nudged elastic band (NEB) method[55] with at least 8 intermediate images and a force convergence threshold of 0.05 eV/Å. All TS were confirmed by further frequency calculations. The vibrational frequencies were calculated by a finite difference approach with a 0.015 Å displacement for each degree of freedom. Only one imaginary frequency was found for each TS structure, while only positive frequencies characterized the intermediates.

The calculated relative Gibbs free energy (ΔG), either the reaction energy ($\Delta_r G$) or the adsorption energy ($\Delta_{ads} G$), was evaluated as $\Delta G = \Delta E_{DFT} + ZPE + \int_0^T C_p\left(T'\right)dT' - T\Delta S$, following the work by Bendavid and Carter.[56] E_{DFT}, ZPE, C_p, T, and S are the DFT electronic energy, zero-point energy, heat capacity, temperature, and entropy, respectively. These properties were calculated from the vibrational modes of the bound systems and the gas-phase molecules at 298.15 K and 101.3 kPa, as implemented in the VaspGibbs code.[57] The activation energies were calculated as $G_a = G_{TS} - G_{IS}$, in which G_{TS} and G_{IS} represent the Gibbs energies of the transition and initial states, respectively. The reaction energies were calculated as $\Delta_r G = G_{FS} - G_{IS}$, where G_{FS} is the energy of the final state.

EXPERIMENTAL SECTION

Synthesis of Ag_3PO_4 Microcrystals. Ag_3PO_4 was prepared by a facile coprecipitation (CP) method. In a typical procedure, two solutions were designed: (i) 1×10^{-3} mol of NaH_2PO_4 (J.T.Baker, 98.6%) was dissolved in 50 mL of distilled water in a beaker under magnetic stirring, and (ii) 3×10^{-3} mol of $AgNO_3$ (Cennabras, 99.8%) was dissolved in 50 mL of distilled water in a beaker. In the solution of $AgNO_3$, NH_4OH (Synth, 27%) was added dropwise until the complete complexation of the Ag^+ with ammonia, forming a brown staining precipitate first and, due to an excess of NH_4OH, transforming it into a solution again. After this process, solution (ii) was added to solution (i) to form a yellow precipitate. The precipitate was washed to neutral pH with water and dried at 60 °C.

Materials Characterization. The samples were characterized using X-ray diffraction (XRD) with a D/Max-2500PC diffractometer (Rigaku, Japan) involving Cu Kα radiation (λ = 1.54056 Å) in the 10−80° 2θ range at a scan rate of 0.01° min^{-1}. Micro-Raman spectroscopy was carried out using an iHR550 spectrometer (Horiba Jobin-Yvon, Japan) with a charge-coupled device (CCD) detector and an argon-ion laser (Melles Griot, USA) operating at 633 nm with a power of 200 mW. The spectra were evaluated in the 50−1100 cm^{-1} range. Fourier-transform infrared spectroscopy was carried out on an IRT-3000 spectrometer (Jasco, Japan) over the 600−4000 cm^{-1} range. The FE-SEM images were analyzed by using an FEI instrument (model Inspect F50) operating at 5 kV.

https://doi.org/10.1021/acs.jpcc.3c06321
J. Phys. Chem. C 2023, 127, 23235−23245

As a complementary analysis to XRD, micro-Raman spectroscopy was performed and is shown in Figure 1b. Ag_3PO_4 has 18 active modes in Raman results; however, due to the high degree of disorder of the material, only 4 of these modes are observed, located in 547 (T_2), 709 (T_{2g}), 909 (A_1), and 998 (T_2) cm^{-1}. All of these modes are related to external and internal vibrations of the $[PO_4]$ clusters, with the most intense being the symmetrical stretching of the O−P−O bonds.

The specific vibrations related to Ag_3PO_4 are observed by FT-IR spectroscopy (Figure 1c), indicating no remaining counterions from the synthesis. The vibrations observed at 548, 675, 861, 1023, 1390, and 1547 cm^{-1} refer to the specific stretching and bending vibrations of the P−O and P−O−P bonds of the PO_4^{3-} groups. The band at 2200 cm^{-1} is related to CO_2. No additional bands can be observed, indicating no remnants of groups $(NO_3)^-$ or $(NH_4)^+$ coming from counterions.

Photocatalytic Analysis. The photocatalytic activity of the samples was tested for the degradation of RhB (Aldrich, 95%) in aqueous solutions under visible-light irradiation. This decay occurs due to the xanthene ring (RhB chromophore) undergoing a gradual diethylation in the functional groups of *N,N′*-diethylammonium.[58]

In the experiments, 50 mg of the sample was added into 50 mL (1×10^{-5} mol L^{-1}) of RhB solution in a beaker and placed in an ultrasonic bath for material dispersion into the solution. After this process, the suspension was transferred to an open reactor with water circulation and controlled temperature (20 °C) and left under stirring in the dark for 15 min so that the adsorptive processes dye the sample. Six visible lamps illuminated these solutions (Philips TL-D, 15 W) in a photocatalytic system, and aliquots were withdrawn at predetermined times. The aliquots were centrifuged, and the absorbance variations were measured with a spectrophotometer (V-660 Jasco). In the dark, it was observed that the Ag_3PO_4 sample achieved adsorptive equilibrium with the RhB solution after 5 min of contact. At this point, it ceased to exhibit additional adsorption capacity, already absorbing approximately 10% of the RhB solution (Figure S1a). When the sample was irradiated with light, a gradual decay was observed, which was completed after 10 min of irradiation. Photolysis, the action of light alone, did not show significant degradation, having degraded the RhB solution by approximately 3%.

The degradation process follows first-order kinetics and can be described by $d[C]/dt = k[C]$, where $[C]$ is the RhB concentration and k indicates the rate constant, which can be obtained from the graphical representation of the integrated equation (see Figure S1b). All samples follow the Langmuir−Hinshelwood first-order kinetic fitting model with an excellent fit ($R^2 = 0.99$). A comparison of previously reported k values with this work is given in Table S1.

Scavenger experiments were performed to find the key active species during the photocatalytic activity (Figure S1d). A total of 50.0 mg of each sample was added in equimolar amounts: ammonium oxalate (AO, $(NH_4)_2C_2O_4{\cdot}H_2O$; 99.5%, Aldrich), *p*-benzoquinone (BQ, $C_6H_4O_2$, Merck), silver nitrate (SN, $AgNO_3$, 99.8%, Vetec), and ascorbic acid (AA, $HC_6H_7O_6$; 99.5%, Aldrich), acting as scavengers for h^+, $\bullet O_2^-$, e^-, and •OH, respectively. These equivalent amounts were added to 50.0 mL of a Rhodamine B (RhB, $C_{28}H_{31}ClN_2O_3$, 99.8%, Synth) solution (1×10^{-5} mol L^{-1}), and the same process of photocatalysis was performed. As shown in Figure S1d, the RhB partially disappeared (in the range of 35−65%) when these scavengers were added, which indicated that these four ROS (•OH, $\bullet O_2^-$, e^-, and h^+) were generated during the degradation process, and $\bullet O_2^-$ was first produced, which may be a significant source of other ROS.

Bactericidal Analysis. The experiments were based on the methodology proposed by the Clinical and Laboratory Standards Institute,[59] using 96-well plates where 100 μL of tryptic soy broth (TSB) was added. Next, 100 μL of the first concentration of the homogenized samples was added in column 1, and 100 μL was transferred to the next well and so on until column 10. In the last column, 100 μL was discarded to obtain the same final volume. After the serial dilution of all samples, 20 μL of the bactericidal suspension (*K. pneumoniae* ATCC 1706, *K. pneumoniae* A54970, *E. coli* ATCC 25922, *S. aureus* ATCC 29213, and *P. aeruginosa* ATCC 27853) was inserted into the test wells. The control groups contained the same components as test wells except for bacteria. The positive growth control had only TSB and the inoculum, while the negative sterility control included only TSB and 20 μL of sterile saline solution. A comparative control was performed using the antibiotic gentamicin. At the end of the preparation, the plates were incubated at 37 °C for 24 h. After this period, 20 μL of the revealing dye was added: 0.04% resazurin Alamar Blue (Sigma-Aldrich) diluted in phosphate-buffered saline (PBS) and filtered for sterilization. After an hour of color change, the plates were read in a Multiskan FC microplate reader (Thermo Scientific) at 600 nm. The test was performed in triplicate on two different occasions. The results are in Figure S2. A comparison of the obtained values consistent with those found in previous works where Ag_3PO_4 was used as an antimicrobial agent follows in Table S2.

RESULTS AND DISCUSSION

Materials Characterization. The XRD pattern analysis shows that the as-synthesized samples have a cubic structure (space group $P\bar{4}3n$) of Ag_3PO_4, with a lattice parameter of 6.026 Å, according to card no. 14000 in the Inorganic Crystal Structure Database (ICSD).[60]

The Ag_3PO_4 structure comprises 4-fold coordinated $[AgO_4]$ and distorted tetrahedral $[PO_4]$ clusters. The XRD, Raman, and FT-IR spectroscopy results are presented in Figure 1 and discussed in more detail in the Methods section. Sample purity is confirmed as no additional XRD peaks or Raman bands are detected. Moreover, FT-IR spectra exhibit bands at 1703 and 3074 cm^{-1}, assigned to the stretching modes of the hydroxyl groups and the bending vibration of H_2O, respectively. These results imply that hydroxyl groups −OH and H_2O are adsorbed on the $Ag_3PO_4(110)$ surface.

An analysis of the FE-SEM micrograph in Figure 1d renders faceted blocklike particles, mainly aggregated with a polydisperse size distribution, smooth surfaces, and well-defined rhombic dodecahedral morphology. This morphology comprises the (110) surface, accounting for 80% of the exposed surface. The measured average particle size was 6.37 ± 2.38 μm. From the calculated values of the surface energy of the (100), (110), and (111) surfaces and Wulff construction, the available morphologies of Ag_3PO_4 are presented in Figure S3 and discussed in Section S2.1 of the Supporting Information (SI).

Photocatalytic Analysis. The Ag_3PO_4 microcrystals completely degraded Rhodamine B (Aldrich, 95%) in aqueous

https://doi.org/10.1021/acs.jpcc.3c06321
J. Phys. Chem. C 2023, 127, 23235−23245

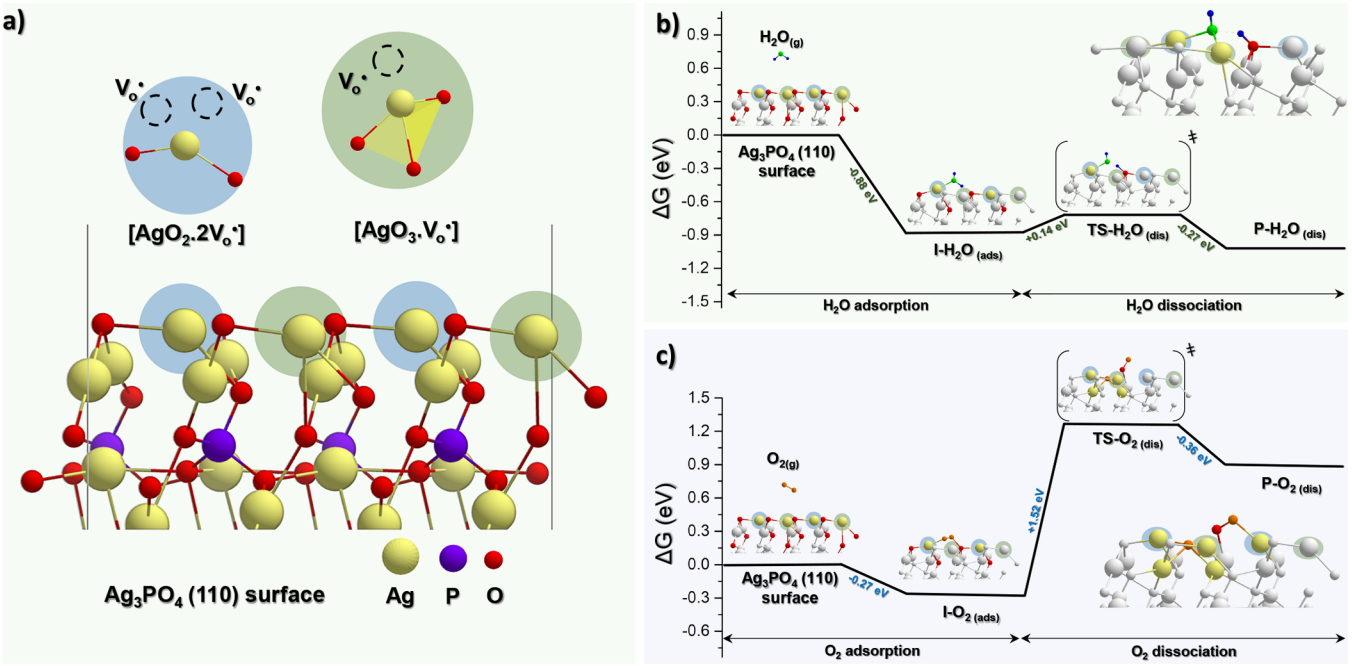

Figure 2. (a) Schematic $Ag_3PO_4(110)$ surface representation. The 3-fold coordinated Ag ($[AgO_3.V_o^{\bullet}]$) and 2-fold coordinated Ag ($[AgO_2.2V_o^{\bullet}]$) are highlighted in green and blue, respectively. The color scheme of the surface atoms is indicated. The free energy profiles of the reaction pathways for dissociating separately (b) H_2O and (c) O_2 on the $Ag_3PO_4(110)$ surface are presented with the Gibbs adsorption energy and relative energy to each consecutive step. Oxygen atoms in O_2 and H_2O are represented by orange and green spheres, respectively. Hydrogen atoms are blue spheres.

solutions under visible-light irradiation in 10 min (Figures S1a). The pseudo-first-order kinetic constant (k) for the degradation of RhB is $k = 0.320\ min^{-1}$ (Figure S1b). Table S1 collects reported values of k for comparison, demonstrating enhanced photocatalytic activity. Subsequently, catalyst recycling was analyzed. After running for three cycles, the as-synthesized samples maintained their high catalytic activity. In the fourth cycle, the material presented good stability, with 84% of the dye being converted to the corresponding product (Figure S1c).

Scavenger experiments were performed to investigate the active species generated in the photocatalytic system. Figure S 1d shows that the photocatalytic degradation was significantly reduced by *tert*-butyl alcohol (TBA) and ammonium oxalate (AO) additives, which quenched •OH and h^+, respectively. Meanwhile, RhB degradation was moderately suppressed by benzoquinone (BQ) and sodium nitrate (SN) as scavengers for $\bullet O_2^-$ and e^-. These results indicate that •OH and h^+ are the main active species in the dye degradation reactions. However, as it was emphasized by Yuan et al.,[61] the precision of this method for quantitative analysis is inadequate. The inhibition effect of scavengers on the catalytic reaction is related to the antioxidant ability of scavengers and the process of the radical chain reaction. Since most free radical scavengers are antioxidants, they can also be vulnerable to free radical attacks and thus inhibit the oxidation of other substances or disrupt chain reactions. In our case, the generation of the •OH radical is coupled with the formation of $\bullet O_2^-$ via the $Ag_3PO_4(110)$ surface. Therefore, the scavenging effect of BQ on $\bullet O_2^-$ radicals also inhibits the formation of •OH radicals. In this case, the addition of either BQ or TBA will significantly reduce the catalytic reaction rate.

Bactericidal Activity. The analysis of the bactericidal activity (Figure S2) revealed a dose-dependent relationship between the MIC value and the Ag_3PO_4 concentration, resulting in values of 62.5, 250, 250, 250, and 500 μg/mL for bacteria *K. pneumoniae* ATCC 1706, *K. pneumoniae* A54970, *E. coli* ATCC 25922, *S. aureus* ATCC 29213, and *P. aeruginosa* ATCC 27853, respectively. Furthermore, no bacterial growth was observed at any tested concentrations, confirming the antimicrobial activity and suggesting that the MIC is equivalent to the minimum bactericidal concentrations (MBC). Reported values of the MIC in previous works are collected in Table S2, displaying the enhanced antimicrobial activity of as-synthesized Ag_3PO_4 microcrystals.

$Ag_3PO_4(110)$ Surface Model. Our study focuses on creating a well-defined model structure for chemical reactions that occur at the surface. In our case, the $Ag_3PO_4(110)$ surface is predominant at the morphology, making it an ideal proof-of-concept model crystal catalyst for our investigation of the adsorption and activation of the O_2 and H_2O molecules to generate ROS precursors.

Figure 2a illustrates the surface using a ball−stick representation, while Figure S4 depicts the detailed slab parameters. The geometry of the $Ag_3PO_4(110)$ surface can be further divided into two different types of undercoordinated Ag cations compared to the bulk $[AgO_4]$ tetrahedra, namely, pseudotrigonally planar and pseudoangular, with one and two charged oxygen vacancies ($V_o^{\bullet}$, following the Kröger−Vink notation[62]), respectively. In its exposed layer, four clusters are present: two clusters with 3-fold coordinated Ag ($[AgO_3{\cdot}V_o^{\bullet}]$) and two clusters with 2-fold coordinated Ag ($[AgO_2{\cdot}2V_o^{\bullet}]$). A detailed analysis of the electronic properties (Bader charges, electron density topology analysis, density of states, DOS) and structural details are reported in Sections S2.2 and S2.3 of the SI.

We analyzed the H_2O and O_2 homolytic dissociation processes separately and then the coadsorbed dissociative processes. In Methods, we present the computational methods to estimate free energy profiles and localize and characterize

https://doi.org/10.1021/acs.jpcc.3c06321
J. Phys. Chem. C 2023, 127, 23235−23245

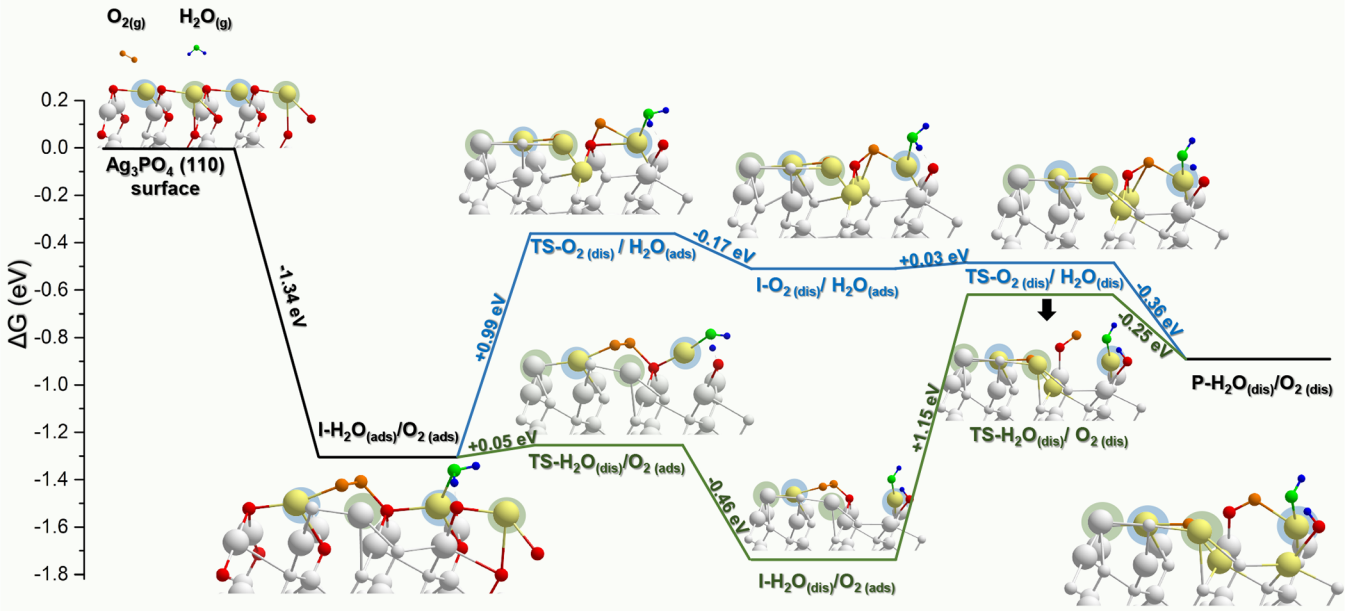

Figure 3. Free energy profiles of the reaction pathways for dissociating coadsorbed H_2O and O_2 on the $Ag_3PO_4(110)$ surface. Pathway initiated by H_2O dissociation (green) and pathway initiated by the O_2 dissociation (blue). Oxygen atoms in O_2 and H_2O are represented by orange and green spheres, respectively. Hydrogen atoms are blue spheres. The Gibbs adsorption energy and relative energy for each consecutive step are presented.

the stationary states along the reaction paths culminating in the formation of ROS precursors. The different adsorption and coadsorption sites for H_2O and O_2 are presented in Section S2.4 (Tables S3, S4, and S6). Section S3 provides the frequency characterization of the transition states (Table S7) and offers structural details of both the transition states and the final intermediates (Figure S8). The structural and electronic properties of the initial adsorption intermediates are detailed in Section S4. Two alternative coadsorption configurations and reaction channels are discussed in Sections S4.3 and S4.4.

Separate Adsorption Processes. Figure 2b presents the free energy profile for the dissociation of H_2O on the $Ag_3PO_4(110)$ surface. Initially, H_2O adsorbs molecularly to form a stable intermediate, $I{-}H_2O_{(ads)}$, with an adsorption free energy $\Delta_{ads}G = -0.88$ eV. In this intermediate, the O atom binds to the Ag cation of one $[AgO_2{\cdot}2\mathbf{V}_o^{\bullet}]$ cluster at an O−H distance of 1.36 Å (Figure S9a).

DOS and crystal overlap Hamilton population (COHP) projected onto the molecule (Figure S9c) disclosed that the nonbonding highest occupied molecular orbital (HOMO) transforms into delocalized antibonding bands upon adsorption. This weakening in the bonding character is revealed through the elongation of the molecular O−H bond from 0.97 to 1.10 Å. The rise of antibonding states is expected to facilitate the electron density transfer from the molecule to more stable surface states. Indeed, Bader charge analysis renders that H_2O mainly acts as an electron donor by transferring 0.10*e* to the surface O anion (Figure S9b).

Subsequently, H_2O homolytic dissociation proceeds through a transition state, $TS{-}H_2O_{(dis)}$, with a mild energy barrier of 0.14 eV and an electron density transfer toward the surface corresponding to a Bader charge of 0.25*e*. The thermodynamics of the reaction strongly favors the dissociation process, as indicated by the free energy change of $\Delta_rG^{\circ} = -0.27$ eV.

Figure 2c depicts the reaction progress from the O_2 adsorption to •O formation on the $Ag_3PO_4(110)$ surface. First, the O_2 molecule chemisorbs on the surface and forms a stable intermediate, $I{-}O_{2(ads)}$, with adsorption free energy of $\Delta_{ads}G = -0.27$ eV. One oxygen atom coordinates with the Ag cation of one $[AgO_2{\cdot}2\mathbf{V}_o^{\bullet}]$ cluster at a Ag−O distance of 2.14 Å, while the other binds with one O anion of an adjacent $[AgO_2{\cdot}2\mathbf{V}_o^{\bullet}]$ cluster (Figure S10a).

DOS and COHP analysis projected onto O_2 (Figure S10d) revealed that the antibonding $2\pi^*$ HOMO transformed into antibonding bands upon adsorption, delineating a discernible electronic reconfiguration. The integration of the COHP indicated that the adsorbate electronic structure presented a remarkable resemblance with that of the gas-phase superoxide radical $\bullet O_2^-$, underscored by the data presented in Tables S4 and S5 and discussed in detail in Section S4.2. The rise of the antibonding bands resulted in the elongation of the molecular O−O bond from 1.23 to 1.29 Å, a geometry that also resembles that of $\bullet O_2^-$ (Tables S5 and S8). Electron density difference analysis (Figure S10b) showed that O_2 accepts electron density from the surface Ag cation, corresponding to a Bader charge of 0.25*e*. Consequently, the magnetic moment of chemisorbed O_2 decreases from 2.0 to 1.0 μB.

From the $I{-}O_{2(ads)}$ intermediate, the homolytic dissociation process of the O_2 involves a high energy barrier of 1.52 eV and leads to a thermodynamically unstable product with high energy ($\Delta_rG = +1.16$ eV), underscoring the practical inaccessibility of this reaction route. In summary, our study reveals that the $Ag_3PO_4(110)$ surface exhibits the preferential chemisorption of H_2O molecules, with electron density transferring from H_2O to the surface. This phenomenon significantly promotes the homolytic dissociation of H_2O, yielding chemisorbed •OH and •H radicals. Conversely, we observed an inverse electron transfer where the surface donates electrons to O_2. Notably, we found that the pathway involving the cleavage of the O−O double bond on the $Ag_3PO_4(110)$ surface is energetically unfavorable, primarily due to the substantial activation energy required for this dissociation process.

https://doi.org/10.1021/acs.jpcc.3c06321
J. Phys. Chem. C 2023, 127, 23235−23245

Coadsorption Processes. Different types of scenarios for the coadsorption of O_2 and H_2O on $Ag_3PO_4(110)$ were investigated (details in Section S2.4). The most favorable to the formation of ROS is when these molecules interact with the Ag cation of adjacent $[AgO_2{\cdot}2V_o^{\bullet}]$ clusters of the $Ag_3PO_4(110)$ surface, which modulates a charge transfer path from H_2O to O_2. Figure 3 displays the free energy profiles for two alternative paths, corresponding to the consecutive dissociation of H_2O and O_2 molecules (green) and vice versa (blue). A third pathway resulted in the formation of a •OOH precursor through hydrogen transfer from chemisorbed H_2O to chemisorbed $\bullet O_2^-$ and is presented in Section S4.4.

The coadsorption of H_2O and O_2 results in a stable intermediate, $I{-}H_2O_{(ads)}/O_{2(ads)}$, with an adsorption free energy of $\Delta_{ads}G = -1.34$ eV. O_2 binds one Ag cation of one $[AgO_2{\cdot}2V_o^{\bullet}]$ cluster and one O anion of an adjacent $[AgO_2{\cdot}2V_o^{\bullet}]$ cluster, whose Ag cation coordinates in turn with the oxygen atom from H_2O. One of its hydrogen atoms also establishes a bond with an O anion of one adjacent $[AgO_3{\cdot}V_o^{\bullet}]$ cluster. This geometry is depicted in Figure 4a.

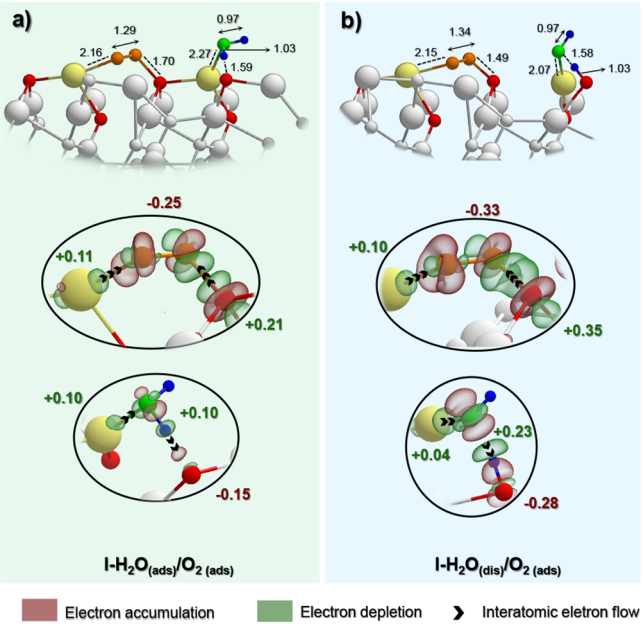

Figure 4. Coadsorption of O_2 and H_2O on the $Ag_3PO_4(110)$ surface, (a) before and (b) after H_2O dissociation. Oxygen atoms in O_2 and H_2O are represented by orange and green spheres, respectively. Hydrogen atoms are blue spheres. Insets show the charge density difference for each configuration, with an isosurface value of 0.007 e $Å^{-3}$. Bader charges (e) are assigned to each molecule or atom relative to their values in the isolated molecule or on the pristine surface. Distances are measured in Å.

The trends in electron density transfer and structural modifications observed for the molecules separately are similar to the ones displayed by each molecule in turn when coadsorbed. H_2O acts as an electron donor, yielding a mean Bader charge of 0.10*e* to the surface of the O anion, resulting in the elongation of the O−H molecular bond from 0.97 to 1.03 Å. O_2 simultaneously acts as an acceptor, capturing a Bader charge of 0.25*e* from the surface. The 0.91 value for the ratio of spin-resolved integrated COHP of the chemisorbed species exhibited a marked resemblance with that of 0.90 for gas-phase $\bullet O_2^-$ (Tables S5 and S6), as its total magnetic moment, which decreased from 2.00 to 1.00 μ_B, and bond length, which increased from 1.23 to 1.29 Å

Subsequently (green path), we find that H_2O homolytic dissociation is thermodynamically favorable, with a reaction free energy (Δ_rG) of −0.46 eV. This process yields the most stable intermediate among all of the reaction pathways under consideration, composed of chemisorbed $\bullet O_2^-$, •OH, and •H. This favorable transformation proceeds through a transition state denoted as $TS\text{-}H_2O_{(dis)}/O_{2(ads)}$, which significantly lowers the energy barrier, reducing it from 0.14 to 0.05 eV when compared to the energy barrier observed in the H_2O separate adsorption process.

The formation of •OH and •H increases the electron density transferred toward the surface, corresponding to the rise of Bader charge from 0.10 to 0.23*e* (see insets of Figure 4a,b) when compared to the initial adsorptive configuration ($I{-}H_2O_{(ads)}/O_{2(ads)}$). A 0.33*e* increase in the O_2 charge with corresponding charge depletion in its surface binding sites is also seen and results in the lengthening of the O−O bond in the molecule to 1.34 Å. We expect these opposite charge transfer processes to set in motion a synergic effect. The depletion of surface electrons caused by the acceptor group should create a favorable local potential in the surface that helps it harness new electrons from the donor group. This should result in a coupled mechanism between H_2O and O_2 that mutually benefits their activation. The observed increase in the total negative charge of the O_2 and the further lengthening of its bond, when compared to the scenario in which there is no donor group, are possible outcomes of such an effect.

After H_2O dissociates generating bound •OH and •H, the coadsorbed oxygen species are in an activated form resembling $\bullet O_2^-$. Probing for the possibility of its complete homolytic dissociation, we found it to be energetically unfavorable with $\Delta_rG = +0.86$ eV and a substantial activation barrier of 1.15 eV. The dissociative product, $P{-}H_2O_{(dis)}/O_{2(dis)}$, consists of chemisorbed •OH, •H, and •O radicals. Notably, both the energy barrier and reaction energy for O_2 homolytic dissociation are lower in the presence of coadsorbed H_2O. We infer that the presence of H_2O acting as an electron donor is fundamental to supply the increased charge that benefits the scission of the O_2 bond.

From the initial coadsorptive and nondissociated configuration, $I{-}H_2O_{(ads)}/O_{2(ads)}$, an alternative reaction pathway emerges where the dissociation of O_2 precedes the cleavage of the H_2O bond (blue pathway in Figure 3). The O_2 dissociation is an endergonic process ($\Delta_rG = +0.82$ eV) but exhibits a reduced energy barrier of 0.99 eV, highlighting the beneficial role of coadsorbed H_2O for the O_2 bond cleavage, which is in effect even before the formation of •OH radicals. Subsequently, H_2O dissociates with a low barrier of 0.03 eV.

However, it is important to note that this entire alternate reaction route follows a high-energy path in comparison to the other possible reaction channel (green pathway in Figure 3). Therefore, the most favorable scenario for generating ROS precursors at the $Ag_3PO_4(110)$ surface involves the consecutive dissociation of H_2O and O_2.

The rationale behind the observed outcomes becomes evident through a comprehensive examination of the conduction band (CB) positioning and composition on the $Ag_3PO_4(110)$ surface, alongside the HOMO characteristics of both H_2O and O_2 molecules. The CB encompasses the 4d orbitals of undercoordinated Ag cations and the 2p orbitals of

https://doi.org/10.1021/acs.jpcc.3c06321
J. Phys. Chem. C 2023, 127, 23235−23245

O anions within both $[AgO_2{\cdot}2V_o^{\bullet}]$ and $[AgO_3{\cdot}V_o^{\bullet}]$ clusters. The diminished coordination of Ag cations results in an electron depletion of the surface states (see Section S2.3.3 for a detailed account) that culminates in the emergence of low-energy CB states contiguous with the Fermi level, as depicted in Figure S7.

The HOMO of H_2O, constituted by the 2p orbitals occupied by the lone electron pairs of the oxygen atom, effectively hybridizes the low-energy CB states. As a result, the sharply localized nonbonding HOMO broadens into antibonding delocalized bands. This transformation facilitates the electron transfer from the molecule to populate the low-energy CB states and culminates in the creation of chemisorbed •OH at the surface.

Furthermore, the surface's CB and the partially occupied HOMO of O_2, characterized by molecular $2\pi^*$ orbitals, also engage in an effective coupling mechanism. This interaction leads to the hybridization of the antibonding HOMO into antibonding bands that shift energy levels downward in a broad range, positioning themselves beneath both the Fermi level and the newly populated surface CB. This strategic arrangement facilitates the capture of electrons transferred from the surface, giving rise to the precursor of the superoxide anion radical, $\bullet O_2^-$. Based on the above analysis, the mechanism can be schematically displayed in Figure 5.

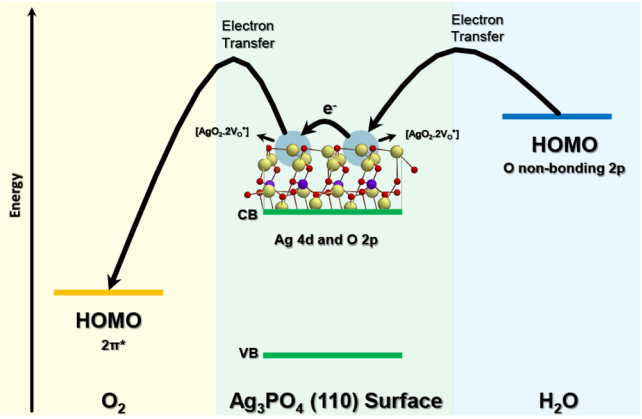

Figure 5. Schematic representation of the position for HOMO-H_2O, CB, and VB of the $Ag_3PO_4(110)$ surface and HOMO-O_2. The electron transfer pathway associated with generating $\bullet O_2^-$ and •OH is highlighted.

The DFT findings suggest that the shallow unfilled CB states that emerge from the undercoordinated Ag-centered clusters in the $Ag_3PO_4(110)$ surface promote the electron transfer pathway between coadsorbed H_2O to O_2. This a crucial step in the activation process that culminates in the cleavage of molecular O−H and O−O bonds at $[AgO_2{\cdot}2V_o^{\bullet}]$ clusters, which act as active centers. We identified the limiting factor for the continued activation of O_2 up to its homolytic dissociation to be the total number of electrons that it can harness from the surface. The presence of the donor H_2O as an electron donor group can increase this number. We expect that this electron donor/acceptor molecule pair coupling through a medium that offers a low-energy path to modulate the electron transfer is a suitable solution to kinetic bottleneck issues in the dissociation of any of these molecules.

Additionally, the release of chemisorbed $\bullet O_2^-$ and •OH intermediates should be optimized to enhance catalytic activity since our calculations revealed that an input of over 3 eV is required for the desorption process. Particularly, the surface is covered to some degree by water and dissociated hydroxyl groups, according to FT-IR data. Whereas these donor groups should improve the oxidation of the O_2 group, they can also constitute a steric hindrance for further ROS formation, as both molecules compete for the same adsorption sites.

The most stable structure along the free energy profiles involves the formation of chemisorbed $\bullet O_2^-$ and •OH ROS precursors. In this configuration, the system composed of surface and bound moieties becomes energetically stable, and the dissociative chemisorption of H_2O is promoted. The stability of these species on the $Ag_3PO_4(110)$ surface is the origin of the enhanced photocatalytic and biocidal activities. In contact with organic molecules or bacteria, these chemisorbed highly reactive moieties react chemically, resulting in the degradation of organic molecules or the inactivation of bacteria, respectively.

Additionally, forming these reactive radicals may lead to the generation of other chemisorbed ROS. We found a reaction path involving the hydrogen transfer from chemisorbed H_2O to O_2 with concomitant formation of the precursor of the chemisorbed perhydroxyl radical, •OOH, by the protonation of $\bullet O_2^-$. However, the TS of this process displays a considerable activation barrier of 0.43 eV in an endergonic reaction, whose final intermediate is more unstable than those analyzed in this work. More details about this unfavorable channel are presented in Section S4.4.

Hydrogen peroxide, H_2O_2, can be obtained by the successive protonation and reduction of $\bullet O_2^-$ radicals: $\bullet O_2^- + 2H^+ + e^- \rightarrow H_2O_2$ or by the combination of two •OH radicals: •OH+ •OH $\rightarrow H_2O_2$. A singlet oxygen molecule, $^1O_2$, can be generated by oxidation of chemisorbed $\bullet O_2^-$: $\bullet O_2^- \rightarrow {}^1O_2 + e^-$. On the other hand, the source of electrons to activate the chemisorbed O_2 and H_2O molecules can be the lattice oxygen anion, intrinsic oxygen vacancies, or defect sites, which leads to the generation of $\bullet O_2^-$ and •OH, respectively. Henceforward, these stored electrons can improve the reduction of •OH to the hydroxyl anion OH^- at the surface. Alternatively, the surface can provide electrons to the adsorbed O_2 molecule and generate $\bullet O_2^-$, O_2^{2-}, and, by breaking the O−O bond, the ionosorbed oxygen species, $\bullet O^-$, until $\bullet O^{2-}$ can be formed on the surface.[63] Since the actual reduction and oxidation reactions occur at each adsorbed state, the redox properties may greatly alter depending on the degree of the stabilization energy by the adsorption and the presence of intrinsic oxygen vacancies and defects.

Before we conclude, we acknowledge that our research was conducted using an intuitive model, in which the catalysts are described by using an extended $Ag_3PO_4(110)$ slab as the predominant exposed surface at the morphology of the as-synthesized Ag_3PO_4 samples. This is an oversimplified yet valuable picture that cannot fully replicate all of the features of the Ag_3PO_4 semiconductor. More complex models for further investigation can be designed based on these findings, which highlight the role of the $Ag_3PO_4(110)$ surface as an active system. The proposed charge dynamics between donor H_2O and acceptor O_2 that we inferred from static data could be further developed and improved via a molecular dynamics study. Nevertheless, our results demonstrated that the energy profiles are qualitatively accurate to likely draw important features once both molecules become trapped on the surface,

https://doi.org/10.1021/acs.jpcc.3c06321
J. Phys. Chem. C 2023, 127, 23235−23245

significantly contributing to the increased production of chemisorbed •OH and $•O_2^-$ radicals as ROS precursors.

Therefore, we identify several aspects that must be considered to realize an accurate and physically meaningful description of photocatalysis and biocide activity. First, the limitations of the static DFT calculations, which provide somewhat limited information about the properties of the relevant excited states, motivate more realistic calculations, including both atom and electron dynamics. Second, it is essential to understand that the morphology can change with outside factors like temperature, presence of oxidizing or reducing agents, etc., affecting its characteristics to limit the use of the present $Ag_3PO_4(110)$ surface model.

Further studies require the application of more accurate electronic structure calculations with periodic methods and advanced embedding schemes to understand more thoroughly the interactions among adsorbates, electron density distributions, and active catalytic sites. Such an expedition would undoubtedly help advance the knowledge of feasible and operative elementary steps on other semiconductor surfaces. We anticipate this trend to continue.

CONCLUSIONS

In this work, the combination of experimental and theoretical results was shown to be a practical approach for revealing an unprecedented mechanism to disclose the formation of the precursors of ROS: chemically adsorbed $•O_2^-$ and •OH radicals. Benefiting from its unique spatial and electronic structure, the $Ag_3PO_4(110)$ surface acts as an electron donor and acceptor. It behaves as a conductive bridge, enhancing an electron transfer-dominated pathway from H_2O to O_2. Undercoordinated Ag cations and positive oxygen vacancies were observed at $[AgO_2{\cdot}2V_o^{\bullet}]$ clusters constructing this dual activity so that the nature of the CB of the $Ag_3PO_4(110)$ surface promotes the realization of a reaction pathway with the lowest energy barrier and enables the chemisorption and homolytic dissociation of H_2O and O_2 at the $Ag_3PO_4(110)$ surface.

The most stable geometry along the corresponding energy profile corresponds to chemically adsorbed •OH and $•O_2^-$ radicals acting as a reactive intermediate for further reactions. The crucial role of highly reactive species, •OH, is proven by scavenger experiments, which guarantee the enhanced photocatalytic and biocidal activity of as-synthesized Ag_3PO_4 microcrystals.

We show that the unexpected chemical activity of the $Ag_3PO_4(110)$ surface, containing chemisorbed H_2O and O_2 molecules, is governed by structural and electronic features and cannot be correlated to those of the bulk. The emerging picture differs from that in photocatalysis, in which electron−hole pairs are created when UV light is shone to activate O_2 and H_2O. These results offer an alternative entirely new mechanism for rationalizing the catalytic reaction behavior at the atomic and electronic levels. Moreover, the chemisorption and activation of H_2O and O_2 on the $Ag_3PO_4(110)$ surface show a correlation between catalytic performance to generate the corresponding ROS and the properties of frontier molecular orbitals of these molecules and the CB and VB of this surface.

Whereas the initial step of the material's photocatalytic effect, ROS formation, is independent of light irradiation, the subsequent step, as probed by the study of RhB degradation, is largely light-driven, as ROS in the dark could only degrade 10% of the samples. Further studies are required to probe the actual interaction between ROS and target molecules or pathogens.

As a proof of concept, the findings of this study deepen our understanding of the generation of ROS and may provide theoretical guidance for the experimental development of novel and efficient heterogeneous catalysts for realizing organic transformations and other catalytic reactions.

ASSOCIATED CONTENT

Supporting Information

The Supporting Information is available free of charge at https://pubs.acs.org/doi/10.1021/acs.jpcc.3c06321.

Photocatalytic and bactericidal activity data for the synthesized microcrystals; comparative tables of photocatalytic and bactericidal activity reported in the literature for Ag_3PO_4-based materials; validation of PBE results by comparison with PBE+U and HSE functionals; DOS and Bader charge analysis of the model surface; Wulff morphology tree and structural models of reaction intermediates; scanning of potential adsorption sites; DOS, COHP, and charge difference plots of the adsorptive systems; frequency characterization of transition states; details of the alternate coadsorptive reactions routes (PDF)

AUTHOR INFORMATION

Corresponding Authors

Juan Andrés − *Department of Physical and Analytical Chemistry, Universitat Jaume I, Castelló de la Plana 12071, Spain;* orcid.org/0000-0003-0232-3957; Email: andres@qfa.uji.es

Miguel A. San-Miguel − *Department of Physical-Chemistry, Chemistry Institute, Universidade Estadual de Campinas, Campinas 13083-872, Brazil;* orcid.org/0000-0002-6650-7432; Email: smiguel@unicamp.br

Authors

Felipe Lipsky − *Department of Physical-Chemistry, Chemistry Institute, Universidade Estadual de Campinas, Campinas 13083-872, Brazil; Department of Physical and Analytical Chemistry, Universitat Jaume I, Castelló de la Plana 12071, Spain*

Luis Henrique da Silveira Lacerda − *Department of Chemistry, Federal University of Santa Catarina, Florianópolis 88040-900, Brazil;* orcid.org/0000-0001-5926-7074

Lourdes Gracia − *Department of Physical and Analytical Chemistry, Universitat Jaume I, Castelló de la Plana 12071, Spain; Department of Physical Chemistry, University of Valencia, Burjassot 46100, Spain*

Beatriz G. Foschiani − *Center for the Development of Functional Materials, São Carlos Federal University, São Carlos 13565-905, Brazil*

Marcelo Assis − *Department of Physical and Analytical Chemistry, Universitat Jaume I, Castelló de la Plana 12071, Spain;* orcid.org/0000-0003-0355-5565

Mónica Oliva − *Department of Physical and Analytical Chemistry, Universitat Jaume I, Castelló de la Plana 12071, Spain;* orcid.org/0000-0001-6651-7852

https://doi.org/10.1021/acs.jpcc.3c06321
J. Phys. Chem. C 2023, 127, 23235−23245

Elson Longo − *Center for the Development of Functional Materials, São Carlos Federal University, São Carlos 13565-905, Brazil;* orcid.org/0000-0001-8062-7791

Complete contact information is available at: https://pubs.acs.org/10.1021/acs.jpcc.3c06321

Author Contributions

The manuscript was written through the contributions of all authors. All authors have approved the final version of the manuscript.

Notes

The authors declare no competing financial interest.

■ ACKNOWLEDGMENTS

The authors acknowledge support from the São Paulo Research Foundation (FAPESP) for grants 2013/07296-2, 2016/23891-6, 2017/26105-4, and 2020/03780-0; from the Coordenação de Aperfeiçoamento de Pessoal de Nível Superior (CAPES); and the National Council for Scientific and Technological Development (CNPq) for grant 305792/2020-2. This work used computational resources of the Centro Nacional de Processamento de Alto Desempenho em São Paulo (CENAPAD-SP) and Centro de Computação John David Rogers (CCJDR-UNICAMP). L.H.d.S.L. acknowledges the National Laboratory for Scientific Computing (LNCC/MCTI, Brazil) for providing HPC resources of the SDumont supercomputer, which have contributed to the research results reported within this work (URL: http://sdumont.lncc.br). J.A. acknowledges Universitat Jaume I for project UJI-B2022-56 and Generalitat Valenciana (project CIAICO/2021/122) for financially supporting this research. M.A. was supported by the Margarita Salas postdoctoral contract MGS/2021/21 (UP2021-021) financed by the European Union-NextGenerationEU. F.L. was supported by a CAPES-PRINT grant, process number 88887.695471/2022-00, and gratefully acknowledges Dr. Luis A. Cabral from for the insightful discussions that greatly contributed to the success of this work.

■ REFERENCES

(1) Barzilai, S.; Aizenshtein, M.; Mintz, M. H.; Hayun, S. Effect of Adsorbed Oxygen on the Dissociation of Water over Gadolinium Oxide Surfaces: Density Functional Theory Calculations and Experimental Results. *J. Phys. Chem. C* **2020**, *124* (27), 14613−14621.

(2) Zhang, L.; Sit, P. H. L. Ab initio study of the role of oxygen and excess electrons in the degradation of CH3NH3PbI3. *Journal of Materials Chemistry A* **2017**, *5* (19), 9042−9049.

(3) Moritz, D. C.; Ruiz Alvarado, I. A.; Zare Pour, M. A.; Paszuk, A.; Frieß, T.; Runge, E.; Hofmann, J. P.; Hannappel, T.; Schmidt, W. G.; Jaegermann, W. P-Terminated InP (001) Surfaces: Surface Band Bending and Reactivity to Water. *ACS Appl. Mater. Interfaces* **2022**, *14* (41), 47255−47261.

(4) Nosaka, Y.; Nosaka, A. Y. Generation and Detection of Reactive Oxygen Species in Photocatalysis. *Chem. Rev.* **2017**, *117* (17), 11302−11336.

(5) Zhang, L.; Zhu, C.; Huang, R.; Ding, Y.; Ruan, C.; Shen, X. C. Mechanisms of Reactive Oxygen Species Generated by Inorganic Nanomaterials for Cancer Therapeutics. *Front Chem.* **2021**, *9*, No. 630969.

(6) El-Kenawi, A.; Ruffell, B. Inflammation, ROS, and Mutagenesis. *Cancer Cell* **2017**, *32* (6), 727−729.

(7) Zhou, Z.; Song, J.; Nie, L.; Chen, X. Reactive oxygen species generating systems meeting challenges of photodynamic cancer therapy. *Chem. Soc. Rev.* **2016**, *45* (23), 6597−6626.

(8) Yang, B.; Chen, Y.; Shi, J. Reactive Oxygen Species (ROS)-Based Nanomedicine. *Chem. Rev.* **2019**, *119* (8), 4881−4985.

(9) Birben, E.; Sahiner, U. M.; Sackesen, C.; Erzurum, S.; Kalayci, O. Oxidative stress and antioxidant defense. *World Allergy Organ J.* **2012**, *5* (1), 9−19. DOI:

(10) Wang, D.; Zhao, L.; Ma, H.; Zhang, H.; Guo, L. H. Quantitative Analysis of Reactive Oxygen Species Photogenerated on Metal Oxide Nanoparticles and Their Bacteria Toxicity: The Role of Superoxide Radicals. *Environ. Sci. Technol.* **2017**, *51* (17), 10137−10145.

(11) Habibi-Yangjeh, A.; Asadzadeh-Khaneghah, S.; Feizpoor, S.; Rouhi, A. Review on heterogeneous photocatalytic disinfection of waterborne, airborne, and foodborne viruses: Can we win against pathogenic viruses? *J. Colloid Interface Sci.* **2020**, *580*, 503−514.

(12) Truong, P. L.; Kidanemariam, A.; Park, J. A critical innovation of photocatalytic degradation for toxic chemicals and pathogens in air. *Journal of Industrial and Engineering Chemistry* **2021**, *100*, 19−39.

(13) Hodges, B. C.; Cates, E. L.; Kim, J. H. Challenges and prospects of advanced oxidation water treatment processes using catalytic nanomaterials. *Nat. Nanotechnol* **2018**, *13* (8), 642−650.

(14) Nagar, A.; Pradeep, T. Clean Water through Nanotechnology: Needs, Gaps, and Fulfillment. *ACS Nano* **2020**, *14* (6), 6420−6435.

(15) Sharman, W. M.; Allen, C. M.; van Lier, J. E. Role of activated oxygen species in photodynamic therapy. *Methods Enzymol* **2000**, *319*, 376−400.

(16) Yi, Z.; Ye, J.; Kikugawa, N.; Kako, T.; Ouyang, S.; Stuart-Williams, H.; Yang, H.; Cao, J.; Luo, W.; Li, Z.; et al. An orthophosphate semiconductor with photooxidation properties under visible-light irradiation. *Nat. Mater.* **2010**, *9* (7), 559−564.

(17) Martin, D. J.; Liu, G.; Moniz, S. J. A.; Bi, Y.; Beale, A. M.; Ye, J.; Tang, J. Efficient visible driven photocatalyst, silver phosphate: performance, understanding, and perspective. *Chem. Soc. Rev.* **2015**, *44* (21), 7808−7828.

(18) Ma, X.; Yan, J.; Liu, N.; Zhu, L.; Wang, B.; Huang, C.; Lü, H. Effect of relaxation on the energetics and electronic structure of clean Ag3PO4(111) surface*. *Journal of Semiconductors* **2016**, *37* (3), No. 033001.

(19) Trench, A. B.; Machado, T. R.; Gouveia, A. F.; Assis, M.; da Trindade, L. G.; Santos, C.; Perrin, A.; Perrin, C.; Oliva, M.; Andrés, J.; et al. Connecting structural, optical, and electronic properties and photocatalytic activity of Ag3PO4:Mo complemented by DFT calculations. *Applied Catalysis B: Environmental* **2018**, *238*, 198−211.

(20) Oliveira, L. P.; Foggi, C. C. d.; Pimentel, B. N. A. d. S.; Assis, M.; Andrés, J.; Longo, E.; Vergani, C. E. Increasing the photocatalytic and fungicide activities of Ag3PO4 microcrystals under visible-light irradiation. *Ceram. Int.* **2021**, *47* (16), 22604−22614.

(21) Li, X.; Xu, P.; Chen, M.; Zeng, G.; Wang, D.; Chen, F.; Tang, W.; Chen, C.; Zhang, C.; Tan, X. Application of silver phosphate-based photocatalysts: Barriers and solutions. *Chemical Engineering Journal* **2019**, *366*, 339−357.

(22) Lin, Y.; Yang, C.; Wu, S.; Li, X.; Chen, Y.; Yang, W. L. Construction of Built-In Electric Field within Silver Phosphate Photocatalyst for Enhanced Removal of Recalcitrant Organic Pollutants. *Adv. Funct. Mater.* **2020**, *30* (38), 2002918.

(23) Amirulsyafiee, A.; Khan, M. M.; Harunsani, M. H. Ag3PO4 and Ag3PO4−based visible light active photocatalysts: Recent progress, synthesis, and photocatalytic applications. *Catal. Commun.* **2022**, *172*, No. 106556.

(24) Wang, H.; He, L.; Wang, L.; Hu, P.; Guo, L.; Han, X.; Li, J. Facile synthesis of Ag3PO4 tetrapod microcrystals with an increased percentage of exposed {110} facets and highly efficient photocatalytic properties. *CrystEngComm* **2012**, *14* (24), 8342−8344.

(25) Yan, X.; Gao, Q.; Qin, J.; Yang, X.; Li, Y.; Tang, H. Morphology-controlled synthesis of Ag3PO4 microcubes with enhanced visible-light-driven photocatalytic activity. *Ceram. Int.* **2013**, *39* (8), 9715−9720.

(26) Yang, Z.-M.; Liu, Y.-Y.; Xu, L.; Huang, G.-F.; Huang, W.-Q. Facile shape-controllable synthesis of Ag3PO4 photocatalysts. *Mater. Lett.* **2014**, *133*, 139−142.

(27) Zhuang, H.; Chen, X.; Xia, J.; Lu, K.; Huang, W.; Liu, X.; Yu, C.; Yang, K. State-of-the-art progress in Ag3PO4-based photocatalysts: Rational design, regulation and perspective. *Applied Materials Today* **2023**, *31*, No. 101742.
(28) Singh, K.; Gujju, R.; Bandaru, S.; Misra, S.; Babu, K. S.; Puvvada, N. Facet-Dependent Bactericidal Activity of Ag3PO4 Nanostructures against Gram-Positive/Negative Bacteria. *ACS Omega* **2022**, *7* (19), 16616−16628.
(29) Tóth, Z. R.; Debreczeni, D.; Gyulavári, T.; Székely, I.; Todea, M.; Kovács, G.; Focşan, M.; Magyari, K.; Baia, L.; Pap, Z.; et al. Rapid Synthesis Method of Ag(3)PO(4) as Reusable Photocatalytically Active Semiconductor. *Nanomaterials (Basel)* **2023**, *13* (1), 89.
(30) Raudoniene, J.; Skaudzius, R.; Zarkov, A.; Selskis, A.; Karlsson, O.; Kareiva, A.; Garskaite, E. Wet-chemistry synthesis of shape-controlled Ag3PO4 crystals and their 3D surface reconstruction from SEM imagery. *Powder Technol.* **2019**, *345*, 26−34.
(31) Hung, N. M.; Oanh, L. T. M.; Chung, D. P.; Thang, D. V.; Mai, V. T.; Hang, L. T.; Minh, N. V. Tuning the particle size, physical properties, and photocatalytic activity of Ag3PO4 materials by changing the Ag+/ ratio. *Chin. Phys. B* **2023**, *32* (3), No. 038102.
(32) Ke, J.; Zhao, J.; Chi, M.; Wang, M.; Kong, X.; Chang, Q.; Zhou, W.; Long, C.; Zeng, J.; Geng, Z. Facet-dependent electrooxidation of propylene into propylene oxide over Ag3PO4 crystals. *Nat. Commun.* **2022**, *13* (1), 932.
(33) Xia, Q.; Liu, B.; Wang, C.; Shen, T.; Li, S.; Bu, Y.; Zhang, Y.; Lu, Z.; Gao, G. Electrostatic-induced green and precise growth of model catalysts. *Proc. Natl. Acad. Sci. U. S. A.* **2023**, *120* (9), No. e2217256120.
(34) Ribeiro, L. K.; Assis, M.; Lima, L. R.; Coelho, D.; Gonçalves, M. O.; Paiva, R. S.; Moraes, L. N.; Almeida, L. F.; Lipsky, F.; San-Miguel, M. A.; et al. Bioactive Ag3PO4/Polypropylene Composites for Inactivation of SARS-CoV-2 and Other Important Public Health Pathogens. *J. Phys. Chem. B* **2021**, *125* (38), 10866−10875.
(35) Seo, Y.; Park, K.; Hong, Y.; Lee, E. S.; Kim, S. S.; Jung, Y. T.; Park, H.; Kwon, C.; Cho, Y. S.; Huh, Y. D. Reactive-oxygen-species-mediated mechanism for photoinduced antibacterial and antiviral activities of Ag(3)PO(4). *J. Anal Sci. Technol.* **2020**, *11* (1), 21.
(36) Steckiewicz, K. P.; Zwara, J.; Jaskiewicz, M.; Kowalski, S.; Kamysz, W.; Zaleska-Medynska, A.; Inkielewicz-Stepniak, I. Shape-Depended Biological Properties of Ag3PO4Microparticles: Evaluation of Antimicrobial Properties and Cytotoxicity in In Vitro Model—Safety Assessment of Potential Clinical Usage. *Oxid. Med. Cell. Long.* **2019**, *2019*, 1.
(37) Cruz-Filho, J. F.; Costa, T. M. S.; Lima, M. S.; Silva, L. J.; Santos, R. S.; Cavalcante, L. S.; Longo, E.; Luz, G. E. Effect of different synthesis methods on the morphology, optical behavior, and superior photocatalytic performances of Ag3PO4 sub-microcrystals using white-light-emitting diodes. *J. Photochem. Photobiol., A* **2019**, *377*, 14−25.
(38) Chen, X.; Dai, Y.; Wang, X. Methods and mechanism for improvement of photocatalytic activity and stability of Ag3PO4: A review. *J. Alloys Compd.* **2015**, *649*, 910−932.
(39) Botelho, G.; Sczancoski, J. C.; Andres, J.; Gracia, L.; Longo, E. Experimental and Theoretical Study on the Structure, Optical Properties, and Growth of Metallic Silver Nanostructures in Ag3PO4. *J. Phys. Chem. C* **2015**, *119* (11), 6293−6306.
(40) Ma, Z.; Lin, S.; Sa, R.; Li, Q.; Wu, K. A comprehensive understanding of water photooxidation on Ag3PO4 surfaces. *RSC Adv.* **2017**, *7* (39), 23994−24003.
(41) Lipsky, F.; Lacerda, L. H. D. S.; de Lazaro, S. R.; Longo, E.; Andrés, J.; San-Miguel, M. A. Unraveling the relationship between exposed surfaces and the photocatalytic activity of Ag. *RSC Adv.* **2020**, *10* (51), 30640−30649.
(42) Perdew, J. P.; Burke, K.; Ernzerhof, M. Generalized Gradient Approximation Made Simple. *Phys. Rev. Lett.* **1996**, *77* (18), 3865−3868.
(43) Kresse, G.; Joubert, D. From ultrasoft pseudopotentials to the projector augmented-wave method. *Phys. Rev. B* **1999**, *59* (3), 1758−1775.
(44) Blöchl, P. E. Projector augmented-wave method. *Phys. Rev. B* **1994**, *50* (24), 17953−17979.
(45) Kresse, G.; Furthmüller, J. Efficient iterative schemes for ab initio total-energy calculations using a plane-wave basis set. *Phys. Rev. B* **1996**, *54* (16), 11169−11186.
(46) Kresse, G.; Furthmüller, J. Efficiency of ab-initio total energy calculations for metals and semiconductors using a plane-wave basis set. *Comput. Mater. Sci.* **1996**, *6* (1), 15−50.
(47) Grimme, S.; Ehrlich, S.; Goerigk, L. Effect of the damping function in dispersion corrected density functional theory. *J. Comput. Chem.* **2011**, *32* (7), 1456−1465.
(48) Cococcioni, M.; de Gironcoli, S. Linear response approach to the calculation of the effective interaction parameters in the $ \mathrm{LDA}+\mathrm{U}$ method. *Phys. Rev. B* **2005**, *71* (3), No. 035105.
(49) Heyd, J.; Scuseria, G. E.; Ernzerhof, M. Hybrid functionals based on a screened Coulomb potential. *J. Chem. Phys.* **2003**, *118* (18), 8207−8215.
(50) Blöchl, P. E.; Jepsen, O.; Andersen, O. K. Improved tetrahedron method for Brillouin-zone integrations. *Phys. Rev. B* **1994**, *49* (23), 16223−16233.
(51) Wang, V.; Xu, N.; Liu, J.-C.; Tang, G.; Geng, W.-T. VASPKIT: A user-friendly interface facilitating high-throughput computing and analysis using VASP code. *Comput. Phys. Commun.* **2021**, *267*, No. 108033.
(52) Maintz, S.; Deringer, V. L.; Tchougréeff, A. L.; Dronskowski, R. LOBSTER: A tool to extract chemical bonding from plane-wave based DFT. *J. Comput. Chem.* **2016**, *37* (11), 1030−1035.
(53) Yu, M.; Trinkle, D. R. Accurate and efficient algorithm for Bader charge integration. *J. Chem. Phys.* **2011**, *134* (6), No. 064111.
(54) Vega, D.; Almeida, D. AIM-UC: An application for QTAIM analysis. *Journal of Computational Methods in Sciences and Engineering* **2014**, *14*, 131−136.
(55) Henkelman, G.; Jónsson, H. Improved tangent estimate in the nudged elastic band method for finding minimum energy paths and saddle points. *J. Chem. Phys.* **2000**, *113* (22), 9978−9985.
(56) Bendavid, L. I.; Carter, E. A. CO2 Adsorption on Cu2O(111): A DFT+U and DFT-D Study. *J. Phys. Chem. C* **2013**, *117* (49), 26048−26059.
(57) Therrien, F. *VaspGibbs: A simple way to obtain Gibbs free energy from Vasp calculations (v 0.2.*1); Zenodo 2023
(58) Pereira, P. F. S.; Gouveia, A. F.; Assis, M.; de Oliveira, R. C.; Pinatti, I. M.; Penha, M.; Gonçalves, R. F.; Gracia, L.; Andrés, J.; Longo, E. ZnWO 4 nanocrystals: synthesis, morphology, photoluminescence and photocatalytic properties. *Phys. Chem. Chem. Phys.* **2018**, *20* (3), 1923−1937.
(59) Laboratory, C. a.; S, I. Performance Standards for Antimicrobial Susceptibility Testing; *CLSI Suppl.* M100, 2020.
(60) Masse, R.; Tordjman, I.; Durif, A. Affinement de la structure cristalline du monophosphate d'argent Ag3PO4. Existence d'une forme haute témperature. *Z. Kristallograph.* **1976**, *144* (1−6), 76−81.
(61) Yuan, B.; Wu, J.; Qin, N.; Lin, E.; Kang, Z.; Bao, D. Sm-doped Pb(Mg1/3Nb2/3)O3-xPbTiO3 piezocatalyst: Exploring the relationship between piezoelectric property and piezocatalytic activity. *Applied Materials Today* **2019**, *17*, 183−192.
(62) Kröger, F. A.; Vink, H. J. Relations between the Concentrations of Imperfections in Crystalline Solids. In *Solid State Physics*, Seitz, F., Turnbull, D., Eds.; Vol. 3; Academic Press, 1956; pp 307−435.
(63) Gurlo, A. Interplay between O2 and SnO2: Oxygen Ionosorption and Spectroscopic Evidence for Adsorbed Oxygen. *ChemPhysChem* **2006**, *7* (10), 2041−2052.

https://doi.org/10.1021/acs.jpcc.3c06321
J. Phys. Chem. C 2023, 127, 23235−23245